



## Additive manufacturing of degradable metallic scaffolds for material-structure-driven diabetic maxillofacial bone regeneration

Wencheng Song<sup>a,b,c,1</sup>, Danlei Zhao<sup>a,d,\*\*\*,1</sup>, Fengyuan Guo<sup>a,b,c,1</sup>, Jiajia Wang<sup>a,b,c</sup>,  
Yifan Wang<sup>a,b,c</sup>, Xinyuan Wang<sup>a,b,c</sup>, Zhengshuo Han<sup>a,b,c</sup>, Wenjie Fan<sup>a,b,c</sup>, Yijun Liu<sup>a,b,c</sup>,  
Zhi Xu<sup>a,b,c,\*\*</sup>, Lili Chen<sup>a,b,c,\*</sup>

<sup>a</sup> Department of Stomatology, Union Hospital, Tongji Medical College, Huazhong University of Science and Technology, Wuhan, China

<sup>b</sup> School of Stomatology, Tongji Medical College, Huazhong University of Science and Technology, Wuhan, China

<sup>c</sup> Hubei Province Key Laboratory of Oral and Maxillofacial Development and Regeneration, Wuhan, China

<sup>d</sup> Department of Mechanical Engineering, The University of Hong Kong, Hong Kong, China

### ARTICLE INFO

#### Keywords:

Additive manufacturing  
Degradable metallic scaffolds  
Material-structure-driven  
Diabetes mellitus  
Maxillofacial bone regeneration

### ABSTRACT

The regeneration of maxillofacial bone defects associated with diabetes mellitus remains challenging due to the occlusal loading and hyperglycemia microenvironment. Herein, we propose a material-structure-driven strategy through the additive manufacturing of degradable Zn–Mg–Cu gradient scaffolds. The *in situ* alloying of Mg and Cu endows Zn alloy with admirable compressive strength for mechanical support and uniform degradation mode for preventing localized rupture. The scaffolds manifest favorable antibacterial, angiogenic, and osteogenic modulation capacity in mimicked hyperglycemic microenvironment, and Mg and Cu promote osteogenic differentiation in the early and late stages, respectively. In addition, the scaffolds expedite diabetic maxillofacial bone ingrowth and regeneration by combining the metabolic regulation effect of divalent metal cations and the hyperboloid and suitable permeability of the gradient structure. RNA sequencing further reveals that RAC1 might be involved in bone formation by regulating the transport and uptake of glucose related to GLUT1 in osteoblasts, contributing to cell function recovery. Inspired by bone healing and structural cues, this study offers an essential understanding of the designation and underlying mechanisms of the material-structure-driven strategy for diabetic maxillofacial bone regeneration.

### 1. Introduction

Maxillofacial bone defects caused by trauma and disease can result in physiological dysfunction (chewing, speech, and breathing) and psychological harm arising from physiological dysfunction and maxillofacial abnormalities. Due to the aging population and unhealthy diets related with urban living, the prevalence of maxillofacial bone defects associated with diabetes mellitus (DM) continues to surge [1]. DM is a metabolic disorder characterized by hyperglycemia and chronic inflammation. The glucose fluctuation can be detrimental to maxillofacial bone remodeling by producing elevated advanced glycation end product (AGE), reactive oxygen species (ROS), and sustaining

inflammation. The pro-inflammatory microenvironment constrains the osteoblast adhesion and proliferation and impedes their osteogenic differentiation with accelerated senescence [2,3]. In addition, hyperglycemia could suppress the propagation of angiogenic cells [4,5], and induce vessel regression and basement membrane thickening, leading to insufficient tissue oxygenation and impaired cell trafficking [6]. However, the frequent exposure to the oral bacterial environment [7], and chronic inflammatory microenvironment caused by hyperglycemia [8], further increase the risk of bacterial infection and led to a critical failure of maxillofacial bone regeneration. Considering the unsatisfactory results of conventional bone regeneration methods in treating diabetic bone defects, there is a serious need to develop an efficient treatment

Peer review under responsibility of KeAi Communications Co., Ltd.

\* Corresponding author. School of Stomatology, Tongji Medical College, Huazhong University of Science and Technology, Wuhan, China.

\*\* Corresponding author. Department of Stomatology, Union Hospital, Tongji Medical College, Huazhong University of Science and Technology, Wuhan, China.

\*\*\* Corresponding author. Department of Stomatology, Union Hospital, Tongji Medical College, Huazhong University of Science and Technology, Wuhan, China.

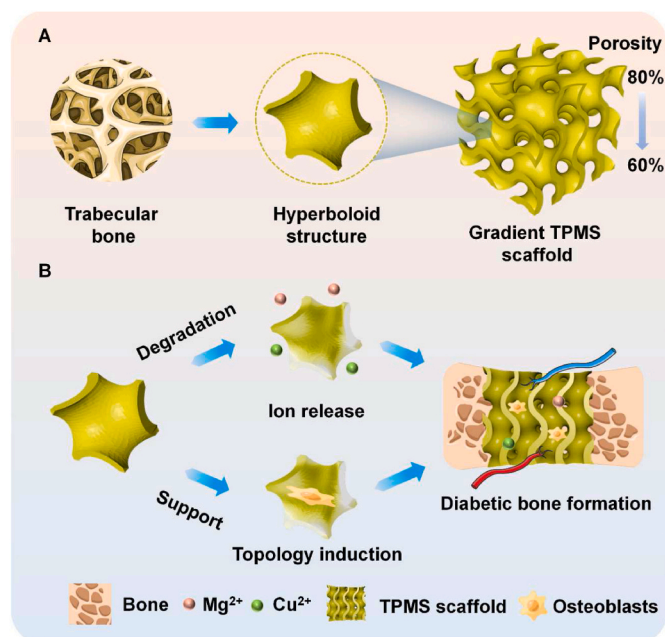
E-mail addresses: [zdihku@hku.hk](mailto:zdihku@hku.hk) (D. Zhao), [xuz@hust.edu.cn](mailto:xuz@hust.edu.cn) (Z. Xu), [chenlili1030@hust.edu.cn](mailto:chenlili1030@hust.edu.cn) (L. Chen).

<sup>1</sup> These authors contributed equally.

<https://doi.org/10.1016/j.bioactmat.2024.06.028>

Received 21 April 2024; Received in revised form 19 June 2024; Accepted 19 June 2024

2452-199X/© 2024 The Authors. Publishing services by Elsevier B.V. on behalf of KeAi Communications Co. Ltd. This is an open access article under the CC BY-NC-ND license (<http://creativecommons.org/licenses/by-nc-nd/4.0/>).



**Scheme 1.** Schematic illustration of the Zn–Mg–Cu gradient scaffold for material-structure-driven diabetic maxillofacial bone regeneration: (A) The hyperboloid structure of the gradient TPMS scaffold inspired by trabecular bone, (B) The ion release and topological structure of the scaffolds can synergistically regulate osteoblast behaviors and functions for diabetic bone formation.

strategy to boost diabetic maxillofacial bone regeneration.

Tissue regenerative medicine can serve as an effective approach for treating maxillofacial bone defects by utilizing degradable bone scaffolds. An ideal biodegradable bone scaffold possesses favorable mechanical properties, a degradation rate comparable to bone regeneration, biological functionality, and a three-dimensional interconnective porous structure. Degradable metals can release divalent metal cations to facilitate bone healing and be gradually absorbed after regenerating bone defects. Li et al. conducted multiscale architecture design of 3D printed biodegradable Zn-based porous scaffolds for immunomodulatory osteogenesis [9]. Zn–Mg alloy draws more attention in orthopedic applications due to its good mechanical strength, suitable degradation rate, and physiological relevance [10]. Wang et al. additively manufactured Zn–2Mg alloy porous scaffolds with customizable biodegradable performance and enhanced osteogenic ability [11]. The release of  $Mg^{2+}$  could induce vascularization by upregulating MagT1 expression in endothelial cells and mimicking the microenvironment of natural bone regeneration [12]. However, the acceleration effect of Mg ion on bone regeneration was time-dependent and particularly pronounced during the initial inflammation phase of osteogenesis [13], which could not satisfy the requirement for biomaterials with relatively long-time pro-osteogenesis in diabetic bone regeneration [14]. Cu was demonstrated to enhance the viability and osteogenic activity of osteoblasts [15], as well as the rigid and self-supporting collagen, which were closely related to bone regeneration [16,17]. Meanwhile, copper (Cu) effectively inhibits bacterial growth and plaque formation, thereby preventing infections and reducing complications such as abscesses, osteomyelitis, and sepsis [15,18,19]. Significantly, the disturbances of Cu ions in serum and bone were found to impact cellular glucose metabolism. The appropriate supplementation of Cu element is beneficial to the recovery of metabolic imbalance and function in peripheral tissue cells [20–22]. Therefore, the incorporation of Cu into Zn alloy might construct an optimal intracellular microenvironment for ossification in hyperglycemia by steering the glucose metabolism and functions of osteoblasts.

Apart from material design, the topological structure of the scaffolds has a significant influence on modulating cell behaviors and functions and remodeling bone defects [23]. The lattice structure of the scaffolds mimicking trabecular bone not only provides Young's modulus matching bone tissue but also induces strengthened bone integration and appealing bone ingrowth [24,25]. Herein, we designed a gradient structure (20%–40 %) with a triply periodic minimal surface lattice (Gyroid-type). The volume fraction varied from 20 % to 40 % along the building direction. Hyperboloidal topography of TPMS can enhance the osteoblasts adhesion and migration and the gradient structure benefits bone ingrowth behavior [26]. Spurred by additive manufacturing, we used laser-powder-bed-fusion (LPBF) to fabricate a Zn–Mg–Cu gradient gyroid scaffold. LPBF can solve the metallurgical challenges between Zn, Mg, and Cu elements while simultaneously preparing a gradient gyroid structure [27,28].

In this work, we propose a material-structure-driven strategy through the additive manufacturing of Zn–Mg–Cu gradient gyroid scaffolds. The Mg and Cu incorporation endows Zn alloy scaffolds with favorable mechanical strength and uniform degradation mode by boundary engineering and *in situ* alloying. The permeability of the gradient gyroid scaffold and the generation of CaP compounds are beneficial for nutrient transportation and osteogenic differentiation, respectively. In addition, Zn–Mg–Cu scaffolds manifest antibacterial, angiogenic, and osteogenic modulation capacity in mimicked hyperglycemic microenvironment and expedite maxillofacial bone formation in diabetic rabbits. RNA sequencing (RNA-seq) reveals that RAC1 might be involved in bone regeneration progress by affecting glucose metabolism in osteoblasts. Inspired by bone healing and structural cues, we explore a material-structure-driven strategy by combining the metabolic regulation effect of divalent metal cations and gradient gyroid structure construction for treating diabetic maxillofacial bone defects (Scheme 1).

## 2. Results

### 2.1. Characterization of the Zn alloy gradient gyroid scaffolds

To achieve material-structure-driven bone regeneration, we utilized laser additive manufacturing (AM) to fabricate degradable Zn alloy gradient gyroid scaffolds. In situ alloying of materials and gradient structure construction can be simultaneously achieved during the AM process. We first inspected the printability, microstructure characteristics, and mechanical behavior of the Zn alloy scaffolds. As shown in Fig. 1A, gradient gyroid scaffolds were prepared from Zn alloy powders with favorable and compact surface transition, producing the hyperboloidal and gradient topology (80 %–60 % porosity). The overall porosities of the printed Zn, Zn–Mg, and Zn–Mg–Cu gyroid scaffolds were calculated to be  $65.83 \pm 1.26 \%$ ,  $67.17 \pm 1.61 \%$ , and  $66.47 \pm 1.50 \%$ , respectively. The average wall thickness of the printed Zn, Zn–Mg, and Zn–Mg–Cu gyroid scaffolds were measured to be  $1.60 \pm 0.08$  mm,  $1.51 \pm 0.13$  mm, and  $1.55 \pm 0.11$  mm, respectively. The gradient designation can enhance penetration capability for nutrients and cells, benefit cellular viability and differentiation, and strengthen mechanical stability [29]. Microstructure analysis reveals that refined cellular and columnar substructures are randomly distributed in the Zn alloys, in contrast to the elongated and coarse lath grains in Zn (Fig. 1B). The inverse pole figures illuminate that the Mg and Cu incorporation decreases the average grain size from  $4.86 \mu\text{m}$  (Zn) to  $1.78 \mu\text{m}$  (Zn–Mg) and  $2.08 \mu\text{m}$  (Zn–Mg–Cu), respectively (Fig. 1C). Meanwhile, the Mg addition dramatically suppressed the peak texture intensity from 10.19 (Zn) to 2.55 (Zn–Mg), as verified by pole figures (Fig. 1D). Moreover, the X-ray diffraction (XRD) spectra of the Zn–Mg and Zn–Mg–Cu reveals the characteristic peaks of  $\alpha$ -Zn and  $Mg_2Zn_{11}$  phase, as depicted in Fig. 1E.

To thoroughly comprehend the strengthening mechanisms induced by alloying elements and the AM technique, the Zn–Mg–Cu alloy was subjected to transmission electron microscope (TEM) observation. Bright-field images reveal the presence of cellular grain, dislocation pile-

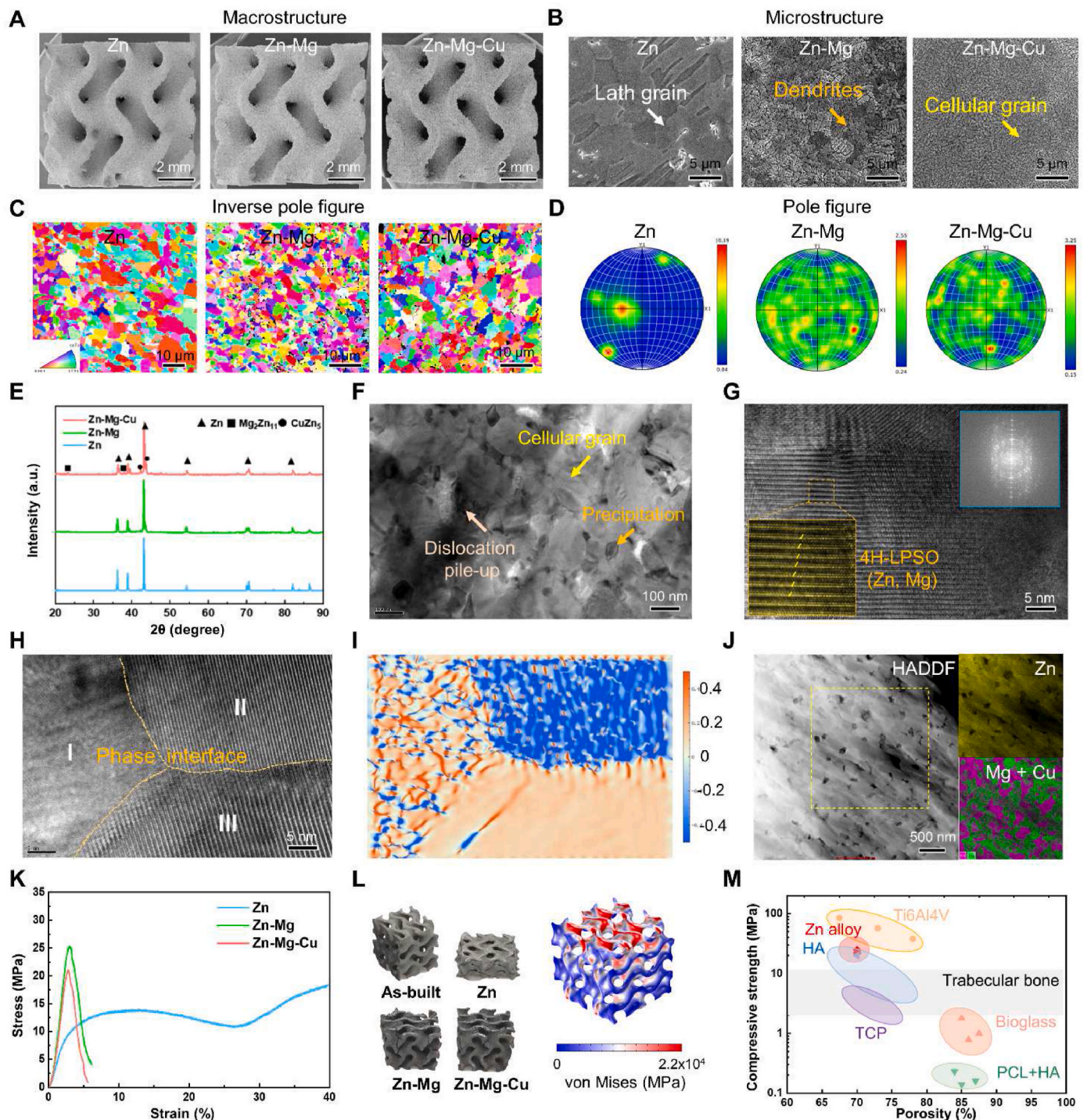


**Fig. 1.** Characterization of the Zn alloy gradient gyroid scaffolds. A–D macrostructure, microstructure, inverse pole figures, and pole figures. E Phase composition. F Bright-field image of the microstructure of Zn–Mg–Cu. G High-resolution TEM (HRTEM) image of Zn–Mg–Cu showing the long period stacking ordered (LPSO) structure and corresponding selected area electron diffraction (SAED) patterns. H–I HRTEM image of Zn–Mg–Cu and corresponding geometric phase analysis (GPA) of the phase interface. J High-angle annular dark-field (HAADF) image of Zn–Mg–Cu and corresponding EDS mapping for Zn, Mg, and Cu elements. K Compressive stress-strain curves. L Visual inspection of the tested scaffolds and stress distribution simulations of the gradient gyroid structure under axial compression using finite element methods. M Porosities and compressive strengths of Zn alloy gradient gyroid scaffolds and other 3D-printed bone scaffolds.

up, and precipitations, indicating the grain boundary and dislocation strengthening (Fig. 1F). In addition, a high-resolution TEM (HRTEM) image of Zn–Mg–Cu shows the 4H-type long-period stacking ordered (LPSO) structure (Fig. 1J) and corresponding selected area electron diffraction (SAED) patterns (Fig. 1G). Geometric-phase analysis (GPA) further displays a high density of lattice distortion neighboring the phase interface of Zn–Mg–Cu alloy (Fig. 1H and I). According to high-

angle annular dark-field (HAADF) images, the Mg and Cu elements are intertwined and uniformly distributed throughout the Zn matrix, suggesting solid solution strengthening. The mappings further demonstrate that AM technology is capable of strengthening the element dissolution in the Zn matrix, mitigating element segregation [30].

Fig. 1K and L depict the stress-strain curves and digital images of the scaffolds following the compression testing. Relative uniform

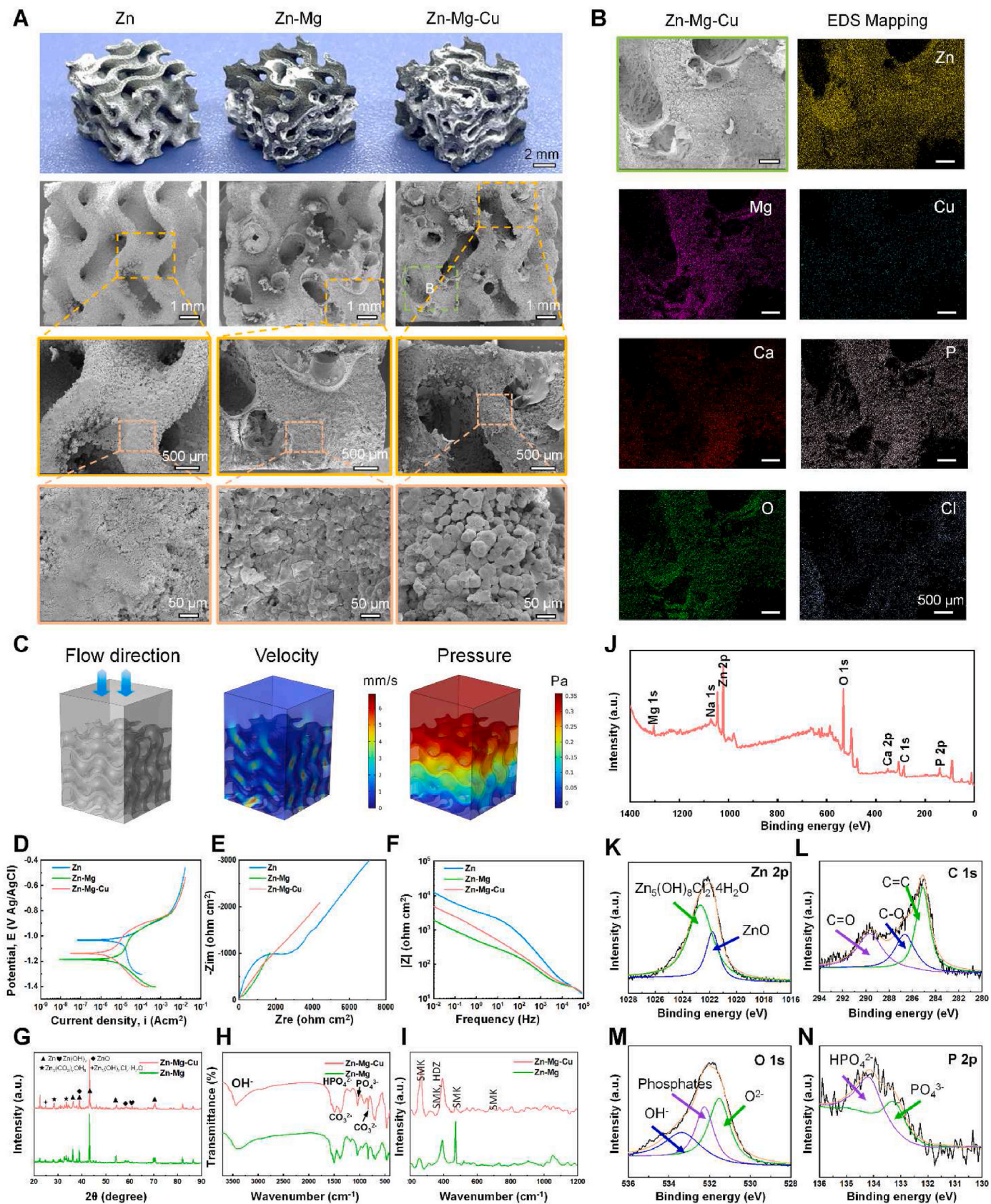
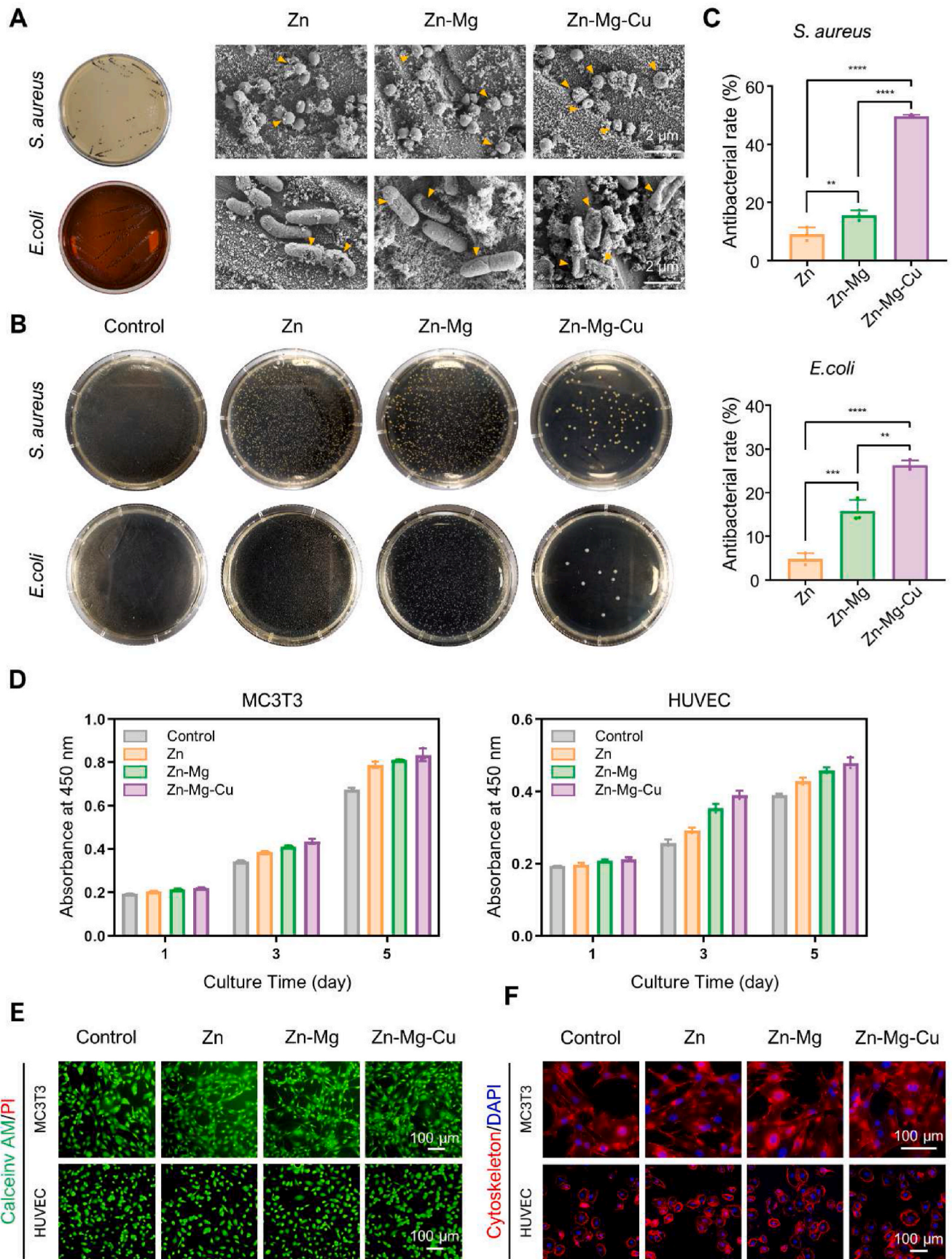


**Fig. 2. Degradation and electrochemical behavior.** A Digital and SEM images depicting the degradation morphology. B EDS mapping results for the degraded Zn–Mg–Cu scaffold. C Geometrical model of the mass-transport simulations, and velocity and pressure contours. D Potentiodynamic polarization (PDP) curves. E Nyquist plots. F Bode plots of the impedance modulus  $|Z|$  vs. frequency. G–I XRD spectra, FTIR spectra, and Raman spectra of the degradation products (SMK:  $\text{Zn}_5(\text{OH})_8\text{Cl}_2 \cdot 4\text{H}_2\text{O}$ ; HDZ:  $\text{Zn}_5(\text{CO}_3)_2(\text{OH})_6$ ). J XPS wide-scan spectrum of the degradation products of Zn–Mg–Cu. K High-resolution XPS spectra of the degraded surface of Zn–Mg–Cu for Zn 2p, C 1s, O 1s, and P 2p.



(caption on next page)

**Fig. 3.** *In vitro* antibacterial and biocompatible performance of the Zn alloys. **A** Identification images of *S. aureus* on the Baird-Parker agar plate and *E. coli* on Eosin-Methylene Blue agar plate. SEM images of morphological alteration of *S. aureus* and *E. coli* incubated with different Zn alloys (The yellow triangles denote the disrupted bacterial membrane), scale bar = 3  $\mu\text{m}$ . **B** Representative photos of *S. aureus* as well as *E. coli* colonies treated with diverse Zn alloys and **(C)** corresponding antimicrobial rate of *S. aureus* and *E. coli*,  $n = 3$ . **D** CCK-8 results of MC3T3-E1 and HUVEC cells cultured with different substrates for 1, 3, and 5 d,  $n = 3$ . **E** Live/dead (Calcein-AM/PI) fluorescence images (scale bar = 100  $\mu\text{m}$ ) and **(F)** morphologies of cells cultured with various Zn alloy extracts for 1 d captured by CLSM (F-actin were stained red, and the cell nuclei were stained blue, scale bar = 100  $\mu\text{m}$ ). The data are shown as the mean  $\pm$  SD; \* $P < 0.05$ , \*\* $P < 0.01$ , and \*\*\* $P < 0.001$  indicate significant differences between the indicated columns.

deformation of the gradient gyroid scaffolds suggests their favorable structural integrity. In addition, the compression simulation result of the gradient gyroid structure corresponded well with the experimental results, revealing the avoidance of substantial stress concentration. Zn–Mg–Cu scaffolds possess a strength of  $21.95 \pm 0.76$  MPa, which is 52.3 % higher than that of the Zn scaffold and matches the compressive strengths of trabecular bone (10–70 MPa). In comparison with the reported data of bone scaffolds, the strength-porosity ratio of Zn alloy gradient gyroid scaffolds surpasses that of other degradable biomaterials and lies between hydroxyapatite and titanium alloys (Fig. 1M) [31–33]. The scaffolds can further fulfill the load-bearing requirements for cancellous bone and cortical bone by adjusting the structure density.

## 2.2. Degradation and electrochemical behavior

We further evaluated the degradation behavior of Zn alloy gradient gyroid scaffolds. White degradation products were visible on the surface of the Zn alloy scaffolds after 28 days of degradation. No apparent partial failure can be observed for all the scaffolds, and Zn–Mg–Cu scaffolds present a more uniform degradation product generation compared with Zn–Mg scaffolds (Fig. 2A). After removing degradation products, the weight loss percentage of Zn, Zn–Mg and Zn–Mg–Cu scaffolds was calculated to be  $7.21 \pm 2.54$  %,  $12.75 \pm 4.16$  % and  $10.26 \pm 3.45$  %, respectively. Compared with Zn, the incorporation of alloying elements accelerates the degradation process. Due to the gradient structure of the scaffold, the degradation rate may vary at different spatial locations. The smooth and continuous surface of sheet-based TPMS structure and more uniform corrosion behavior of Zn–Mg–Cu could reduce the risk of local failure. SEM observation suggests that tiny spherical particles spontaneously formed on the surface of the Zn–Mg–Cu scaffold. Energy-disperse spectrometer (EDS) mappings of the degraded Zn–Mg–Cu scaffold elucidate that the white compounds formed on the strut contain Zn, Ca, O, P, and Cl elements (Fig. 2B). Biomimetic calcium phosphate (CaP) compounds are endowed with biocompatibility and osteoconductivity, which can augment both angiogenesis and bone formation [34].

In addition, we construct a computational fluid dynamics (CFD) model to analyze the mass-transport behavior of the gradient gyroid structure. The permeability and pressure drop are calculated from the CFD simulations, as shown in the velocity and pressure contour (Fig. 2C). The models exhibit an irregular velocity distribution, with the highest velocity found at the pore centers. Most regions possess lower flow velocities ( $< 1.5$  mm/s), providing a suitable environment for cell adhesion and enhancing oxygen transportation. The permeabilities of the structure are  $3.56 \times 10^{-8}$  m<sup>2</sup>, comparable to the reported permeabilities of trabecular bone [35]. Meanwhile, a linear decrease in pressure can be observed along the fluid flow path. The slight pressure drops (0.35 Pa) indicate favorable mass-transport performance, benefiting nutrients supplement and waste metabolism.

To analyze the degradation mode difference induced by alloying elements, we evaluated the electrochemical corrosion features of Zn alloys using potentiodynamic polarization (PDP) and electrochemical impedance spectroscopy (EIS) testing. The corrosion potential of Zn alloys shows shifts toward the negative direction as compared to Zn (Fig. 2D). Nyquist plots (Fig. 2E) suggest that Zn–Mg alloy possesses bigger impedance rings at a low frequency than Zn, indicating an increased corrosion trend. Furthermore, the Cu element increases the impedance rings and associated anti-corrosion tendency. The impedance

modulus at low (0.01 Hz) and medium (10 Hz) frequencies in bode plots further verified the variation rules obtained from Nyquist plots (Fig. 2F). The preceding results illuminate that Mg element exacerbates the corrosion tendency, whereas copper (Cu) mitigates the corrosion trend.

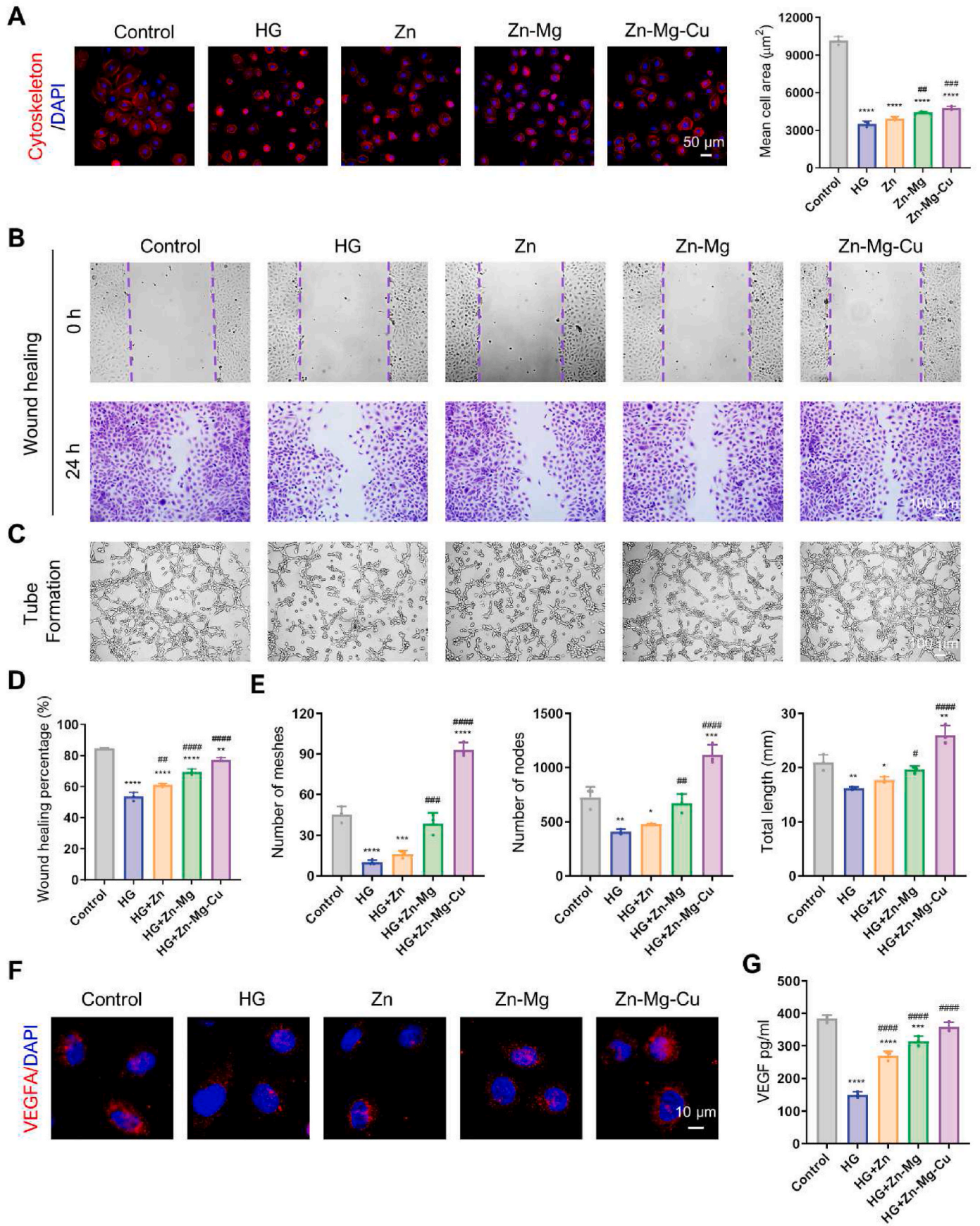
We further use XRD, Fourier Transform-Infrared (FTIR), Raman, and X-ray photoelectron spectroscopy (XPS) to analyze the compositions of the degradation products. The peaks corresponding to ZnO, Zn(OH)<sub>2</sub>, Zn<sub>5</sub>(CO<sub>3</sub>)<sub>2</sub>(OH)<sub>6</sub>, and Zn<sub>5</sub>(OH)<sub>8</sub>Cl<sub>2</sub>·H<sub>2</sub>O (Fig. 2G) can be detected in the XRD spectra. FT-IR spectra reveal the vibration corresponded to Ca<sub>3</sub>(PO<sub>4</sub>)·H<sub>2</sub>O, Zn<sub>5</sub>(OH)<sub>8</sub>Cl<sub>2</sub>·H<sub>2</sub>O, and ZnO (Fig. 2H). Raman spectra further validate the appearance of Zn<sub>5</sub>(OH)<sub>8</sub>Cl<sub>2</sub>·H<sub>2</sub>O and Zn<sub>5</sub>(CO<sub>3</sub>)<sub>2</sub>(OH)<sub>6</sub> (Fig. 2I). Meanwhile, the high-resolution XPS spectra of the degradation products reveal the presence of Zn<sub>5</sub>(OH)<sub>8</sub>Cl<sub>2</sub>·H<sub>2</sub>O, ZnO, and Ca<sub>3</sub>(PO<sub>4</sub>)·H<sub>2</sub>O (Fig. 2K–N).

## 2.3. Antibacterial properties

In the maxillofacial region, bone implants often face more complex microbiological challenges due to the openness of the anatomical site, which can lead to a higher risk of bone regeneration failure [36–38]. As a result, Zn alloy implants have been designed with enhanced antimicrobial properties to effectively manage microorganisms and achieve successful reconstruction of the defects. The antibacterial activity of Zn alloys was assessed against Gram-positive *Staphylococcus aureus* (*S. aureus*) and Gram-negative *Escherichia coli* (*E. coli*). Various Zn alloys were co-cultured with the bacteria, and their morphology was observed using Scanning Electron Microscopy (SEM). It was found that both *S. aureus* and *E. coli* exhibited significant shrinkage and damage when cultured with the Zn–Mg–Cu group (Fig. 3A). Additionally, a bacterial adhesion assay was conducted using the spread plate method. Fig. 3B shows that the agar plate in the control group was almost entirely covered with *S. aureus* and *E. coli* colonies, while the number of colonies on the Zn alloys was significantly lower. Notably, only a few colonies were observed on the Zn–Mg–Cu alloy. After 24 h of exposure to Zn–Mg–Cu eluate, nearly 50 % of *S. aureus* and 25 % of *E. coli* were killed. The antibacterial rate of the Zn–Mg–Cu group showed a significant increase, reaching 4.5 times higher than that of pure Zn and 2.6 times higher than that of the Zn–Mg group (Fig. 3C). These results confirm that the Zn–Mg–Cu group is effective in controlling bacterial infections.

## 2.4. In vitro biocompatibility evaluation

Osteoblasts and endothelial cells play crucial roles in the bone regeneration process and are essential for determining the biocompatibility of implants [39]. In this study, MC3T3-E1, an osteoblast precursor cell line, and HUVEC, an endothelial cell line, were used to evaluate the biocompatibility of Zn alloy implants *in vitro*. MC3T3 and HUVEC cells were co-cultured with various Zn alloy extracts at a 25 % concentration, and OD values were determined at specific time points using the cell counting kit-8 (CCK-8) assay to assess the effect of materials on cell proliferation. Cells incubated with the three Zn alloy extracts exhibited a tendency towards increased proliferation, with the Zn–Mg–Cu group showing the most pronounced proliferative-enhancing potential compared to Zn or Zn–Mg (Fig. 3D). Additionally, the cytotoxicity of different Zn alloys to MC3T3 and HUVEC cells was evaluated using live/dead staining. After 24 h of incubation, virtually no dead cells stained red in all groups, suggesting that Zn alloy implants demonstrated



(caption on next page)

**Fig. 4.** *In vitro* angiogenesis potential of the Zn alloys in mimicked hyperglycemic microenvironment. **A** Morphologies of HUVEC cells treated with diverse Zn alloy extracts for 24 h in mimicked hyperglycemic microenvironment captured by CLSM and corresponding quantitative analysis of mean cell area,  $n = 3$ . **B** Representative images of the scratch wound healing assay at 0 and 24 h and **(D)** corresponding quantification of the percentage of wound healing,  $n = 3$ . **C** Tubular network formation of HUVECs after 6 h of incubation with different Zn alloy medium and **E** quantitative assessment of angiogenic parameters, including the number of meshes, nodes and total length,  $n = 3$ . **F** Representative immunofluorescent images and **(G)** ELISA analysis of VEGFA showing the angiogenesis effect of different Zn alloy extracts on the HUVEC cells. (\* and # represent  $p < 0.05$  when compared with control and HG respectively. \* $p < 0.05$ , \*\* $p < 0.01$ , \*\*\* $p < 0.001$ ; # $p < 0.05$ , ## $p < 0.01$ , ### $p < 0.001$ ).

favorable biocompatibility without any obvious cytotoxic effects (Fig. 3E). These results were supported by CLSM images of cell morphology and cytoskeletal organization (Fig. 3F). Similar to the Zn and Zn–Mg groups, cells in the Zn–Mg–Cu group exhibited early adhesion and spreading with filamentous extensions, indicating good cytocompatibility. Based on the ion concentration in the extracts (Fig. S12), the incorporation of alloying elements facilitates the release of Zn ions, surpassing that of the pure Zn. This phenomenon could potentially explain the enhanced antibacterial properties of Zn–Mg alloy compared to pure Zn. Zn–Mg–Cu alloy contains a comparatively higher amount of Zn and Cu ions relative to the Zn–Mg alloy, which is beneficial for improving antibacterial efficacy, as well as promoting angiogenesis and subsequent osteogenic capabilities.

#### 2.5. *In vitro* angiogenesis potential in mimicked hyperglycemic microenvironment

The process of bone regeneration is closely linked to the process of angiogenesis [40,41]. Blood vessels invade the ossification region to initiate osteogenesis by providing nutrients and secreting essential osteogenesis-related cytokines, such as vascular endothelial growth factor (VEGF) [42]. As a systemic metabolic disease, DM is often accompanied by a variety of vascular dysfunction [43]. HUVEC cells cultured in high-sugar Dulbecco's modified eagle media (DMEM; Hyclone) were used to evaluate the angiogenic performance of Zn alloys in a hyperglycemic microenvironment *in vitro*. Immunofluorescence staining revealed that HUVEC cells in high-glucose environments exhibited poor spreading with a reduced cell spread area. Notably, cell shrinkage induced by high glucose was partially mitigated in all Zn alloy groups, suggesting improved cell viability (Fig. 4A). Based on this observation, wound healing experiments were conducted to assess the *in vitro* migration capacity of HUVECs with varying Zn alloy extracts as depicted in Fig. 4B, the scratch width decreased significantly after incubating with Zn alloy extracts for 24 h compared to the high-glucose group. The healing percentage of the Zn–Mg–Cu group reached 80 %, nearly matching that of the normal group, which highlights its effectiveness in promoting HUVEC migration (Fig. 4D).

We further assessed the angiogenesis-inducing potential of Zn alloys using a tubule formation assay. As seen in Fig. 4C, high glucose hindered tubule formation in HUVEC cells, resulting in fragile and incomplete tubules compared to the control group. After administering Zn–Mg–Cu extracts, more capillary networks with favorable morphological characteristics were observed (Fig. 4C). Quantitative analysis revealed that the corresponding meshes, nodes, and total length were higher than those in other treatment groups, indicating the modulation ability of the Zn–Mg–Cu group to promote vascularization (Fig. 4E). Moreover, the Zn–Mg–Cu group significantly alleviated the inhibitory effect of a high-glucose environment on VEGF protein expression (Fig. 4F–G) and mRNA expressions of VEGFA, FGF1, and FGF2 (Fig. S1A) in HUVECs. This could indirectly promote the osteogenic differentiation of osteoblasts, as demonstrated by the increase in dark blue area and ALP activity (Figs. S1B and C). In conclusion, the Zn–Mg–Cu group enhanced the angiogenic ability of HUVECs in a simulated hyperglycemic microenvironment, creating a favorable setting for long-term bone regeneration.

#### 2.6. *In vitro* osteogenic differentiation of osteoblasts in mimicked hyperglycemic microenvironment

Next, we examined the impact of Zn alloys on the osteogenic differentiation of MC3T3-E1 cells in mimicked hyperglycemic microenvironment using high-glucose media DMEM. ALP (alkaline phosphatase) serves as a key marker of early osteogenesis [44–46]. We first evaluated the functional status of the cells by ALP staining. Representative staining images revealed no significant ALP-positive staining at any time point in the high-glucose (HG) group compared to the control group. In the Zn alloy groups, light blue ALP staining was visible on day 7, and the ALP color deepened after 14 days (Fig. 5A). These observed differences were supported by further quantitative analysis. The ALP activity of the Zn–Mg and Zn–Mg–Cu groups was higher than that of the HG group on day 7, with no significant difference between them. After 14 days, the ALP activity of the Zn–Mg–Cu group surpassed that of the Zn–Mg alloy group, and the difference was statistically significant (Fig. 5B).

Additionally, calcium nodule formation, a later hallmark of osteogenic differentiation, was assessed using Alizarin Red-S (ARS) staining to determine if the Zn alloys can accelerate bone formation in the long term. As expected, the most intense and extensive area of calcium nodules was found in the Zn–Mg–Cu group (Fig. 5A). To further evaluate the osteogenic effect of the Zn alloys at the molecular biological level, a qRT-PCR assay of osteogenesis-related genes was performed. The alloy scaffolds' promotional effect on early osteogenic gene expression was more pronounced on day 7, with the highest upregulation observed in the Zn–Mg group. The Zn–Mg–Cu group demonstrated a strong and sustained bone-promoting effect, as evidenced by the detection of the late osteogenic gene COL1 after 14 days (Fig. 5C). These findings confirm that the osteogenic differentiation capacity is significantly enhanced when Zn, Mg, and Cu work synergistically compared to when used separately. Moreover, osteocalcin, the most abundant osteoblast-specific protein, associated with glucose metabolism of bone formation [47], was demonstrated to increase in MC3T3 cells cultured with the Zn–Mg–Cu extracts by immunofluorescence staining (Fig. 5D, Fig. S9). Furthermore, western blot analysis was performed to estimate the osteogenic differentiation ability of MC3T3 cells on day 14 in mimicked hyperglycemic microenvironment. Compared to Zn and Zn–Mg, Zn–Mg–Cu exhibited higher production levels in terms of osteogenesis-related proteins (RUNX2 and OCN). These results suggest that the significant effects of Zn–Mg–Cu on promoting extracellular matrix mineralization and calcium deposition might be achieved by regulating the glucose metabolism of osteoblasts in a simulated hyperglycemic microenvironment.

#### 2.7. Mechanistic analysis of osteogenic activity induced by the Zn–Mg–Cu alloy implants

To further clarify the underlying mechanism of how the Zn–Mg–Cu alloy activates osteogenesis activity, whole-transcriptome RNA sequencing was performed on MC3T3 cells cultured with HG, Zn–Mg, and Zn–Mg–Cu medium. The Zn–Mg and Zn–Mg–Cu groups were each compared with the HG group to obtain the corresponding sets of differentially expressed genes. Venn analysis of the two differential gene sets revealed that 346 genes were specifically upregulated in the Zn–Mg–Cu group (Fig. 6A). The 346 differentially expressed genes were then analyzed with the Kyoto Encyclopedia of Genes and Genomes (KEGG) pathway enrichment to explore their intrinsic function, and the

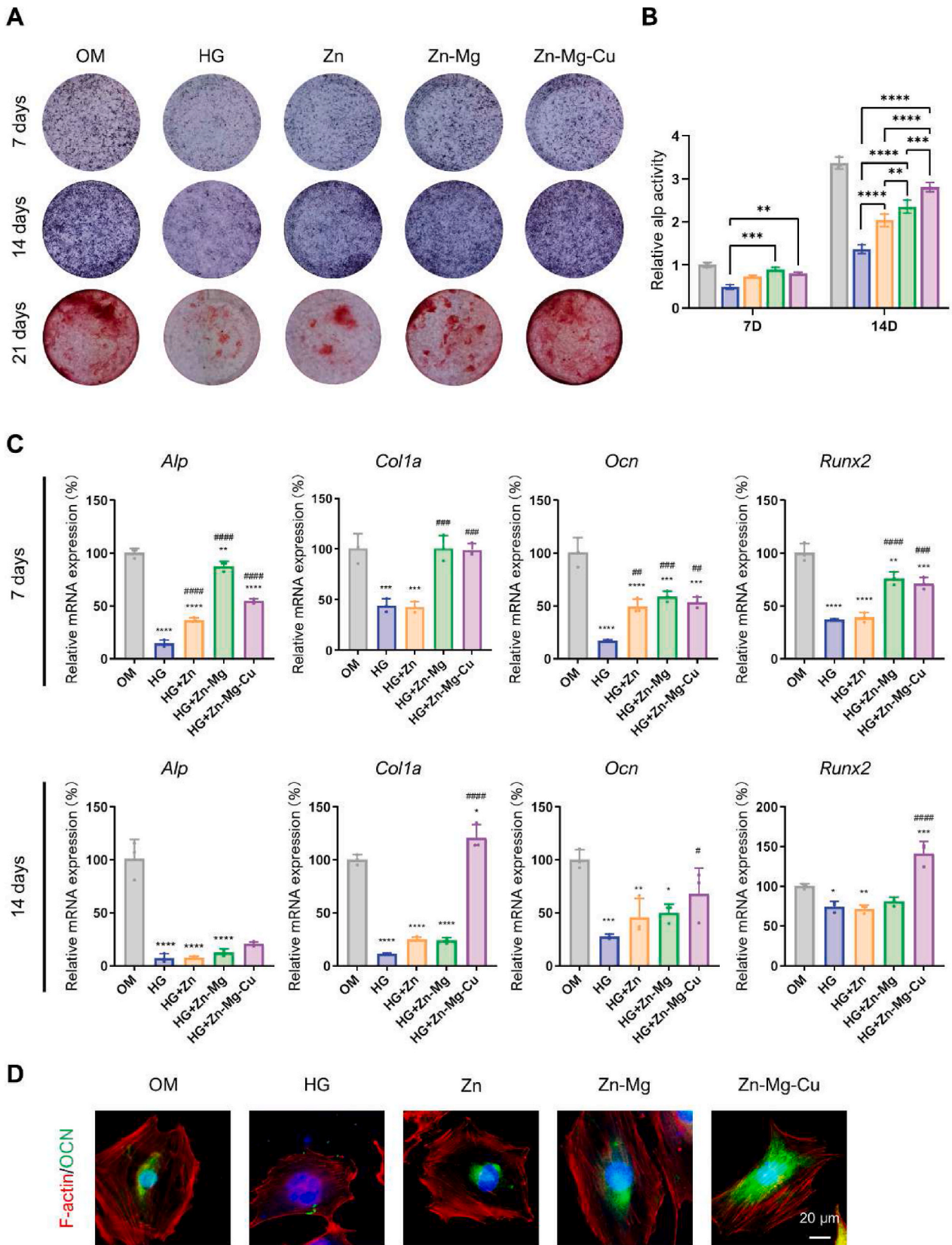
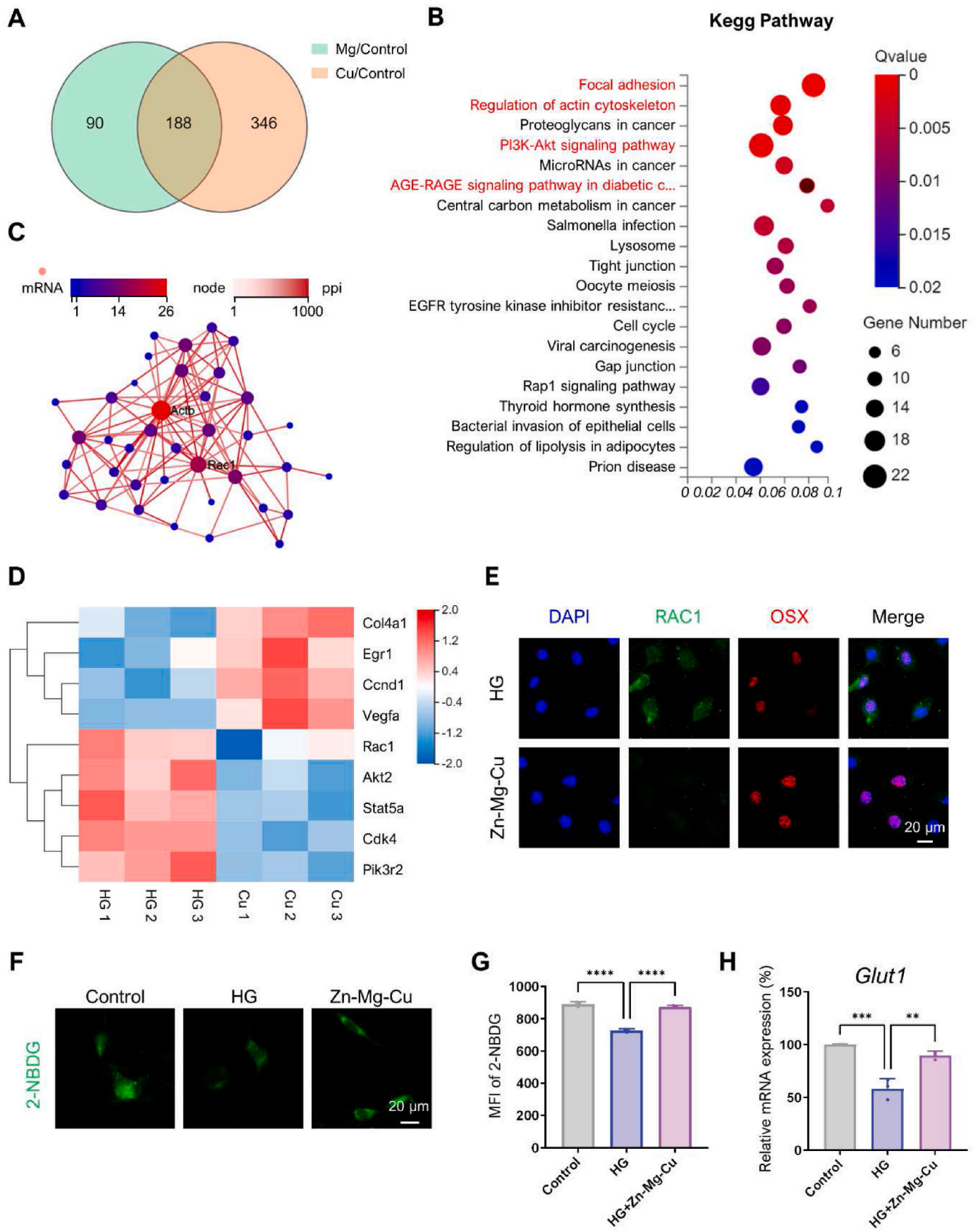


**Fig. 5.** In vitro osteogenic differentiation induced by the Zn alloy implants in mimicked hyperglycemic microenvironment. **A** Representative ALP and Alizarin Red S staining photographs of MC3T3-E1 cells cultured with various Zn alloy medium at each checkpoint and **B** the corresponding quantitative measurement (mean  $\pm$  SD, n = 3). **C** Effect of various Zn alloy extracts on osteogenesis-related gene expression of *Alp*, *Col1 $\alpha$* , *Ocn* and *Runx2* detected on day 7 and 14 by qRT-PCR analysis. **D** Representative OCN immunofluorescent images of MC3T3 (scale = 20  $\mu$ m). The data are shown as the mean  $\pm$  SD; \*P < 0.05, \*\*P < 0.01, \*\*\*P < 0.001, and \*\*\*\*P < 0.0001 compared with Control; # p < 0.05, ## p < 0.01, ### p < 0.001 compared with HG.



(caption on next page)

**Fig. 6. Mechanistic analysis of osteogenic activity induced by the Zn–Mg–Cu alloy in mimicked hyperglycemic microenvironment.** A Venn diagram of differentially expressed genes specific to the Zn–Mg–Cu group that are distinct from the Zn–Mg group versus the control group. B KEGG pathway enrichment analyses of 346 different genes from Venn analysis. C Interaction networks of related genes among focal adhesion, regulation of actin cytoskeleton, PI3K/AKT pathway, and AGE-RAGE signaling pathway. D Heatmap analysis of differentially expressed genes MC3T3 in high glucose group and Zn–Mg–Cu. E Representative immunofluorescence images showing RAC1 and OSX expression in MC3T3 cells following incubation in high glucose group or Zn–Mg–Cu. F 2-NBDG uptake in MC3T3 cells cultured with Zn–Mg–Cu extracts in mimicked hyperglycemic microenvironment was estimated by immunofluorescence (F) and quantitative analysis of flow cytometry assays (G). H The glucose transport involved gene Glut1 expression via qRT-PCR analysis on 3 d. The data are shown as the mean  $\pm$  SD; \* $P < 0.05$ , \*\* $P < 0.01$ , and \*\*\* $P < 0.001$  indicate significant differences between the indicated columns.

top 20 enriched terms are shown in Fig. 6B. We noted that the pathways most related to diabetes and osteogenesis functions (focal adhesion, regulation of actin cytoskeleton, PI3K/AKT signaling pathway, and AGE-RAGE signaling pathway in diabetic complications) were among the top terms (Fig. 6B). The interaction between related genes among the four signaling pathways of interest was visualized by mapping the network for further analysis (Fig. 6C), and the top 9 genes with the most distinct expression differences were listed in a heatmap (Fig. 6D).

Notably, RAC1, which is associated with the four aforementioned pathways, has been reported to play a key regulatory role in glucose metabolism and insulin function. Its activity has been found to increase in individuals with diabetes [48,49]. Based on this, we speculate that RAC1 may play a coordinating role in promoting osteogenesis by alloy scaffolds. Treatment with Zn–Mg–Cu extracts reduced the expression of RAC1 induced by high glucose, which was validated by western blotting and qRT-PCR results (Figs. S2A–C). Immunofluorescence staining showed low RAC1 expression in cells with positive OSX in the Zn–Mg–Cu group, suggesting a potential association between these two molecules. We further measured the level of glucose metabolism via immunofluorescence and flow cytometry analysis. As shown in Fig. 6F–G, MC3T3 cells in the Zn–Mg–Cu group had significantly higher 2-NBDG uptake capacity, while a visible inhibition effect was observed in the HG group. In line with the 2-NBDG uptake results, the expression of the major glucose transporter GLUT1 in osteoblasts was upregulated by Zn–Mg–Cu, as indicated by qRT-PCR analysis (Fig. 6H). Together, these results suggest that incubation with Zn–Mg–Cu extract might promote the glucose uptake capacity of osteoblasts by regulating the expression of RAC1, thereby supplying energy for the differentiation of osteoblasts and promoting bone regeneration under a high glucose environment.

### 2.8. *In vivo* evaluation of bone regeneration induced by Zn alloy scaffolds in diabetic rabbit mandibular defects

Encouraged by the *in vitro* cell experiments, implantation was performed to test the biosafety and pro-osteogenic effect of different Zn alloy scaffolds under DM conditions. To do this, we established a mandibular defect model on diabetic rabbits. These diabetic rabbits were humanely sacrificed at 4 and 12 weeks postoperatively, and the mandibles were harvested for further analysis (Figs. S3A–D). Micro-CT scanning was performed to observe the new bone formation outcomes of mandible bone defects. The 3D reconstruction and coronal images of the mandible defect showed the penetration and growth of new bone into the porous structure of Zn alloy scaffolds, while marked bone depressions were observed in the diabetic group without implantation (Fig. 7A). The quantitative analysis of the micro-CT reconstruction images of newborn trabecular bone depicted the bone mineral density (BMD), bone volume/tissue volume (BV/TV), trabecular bone thickness (Tb. Th), trabecular number (Tb-N) and trabecular separation (Tb. Sp) (Fig. 7B; Fig. S4–9). The new bone surrounding the Zn–Mg and Zn–Mg–Cu scaffolds was significantly more extensive than the Zn implant at 4 weeks after implantation, according to the quantitative micro-CT analysis and reconstructed images. With time extended to 12 weeks, the largest newborn bone volume (about 45 mm<sup>3</sup>) and the highest bone-implant contact rate were detected in the Zn–Mg–Cu group, suggesting that the Zn–Mg–Cu scaffolds had the strongest *in vivo* osteogenicity in diabetic rabbits. Besides, implants are suggested to

provide mechanical support for at least 12–24 weeks depending on the clinical conditions, although the bone healing time varies for different defect sites [50]. *In vivo* degradation behavior of Zn–Mg–Cu implants was evaluated utilizing Micro-CT. At 12 weeks, the volume of Zn–Mg–Cu implant dropped to 82.13  $\pm$  4.5 % (n = 3) and its degradation rate was 3.57  $\pm$  0.9 mm<sup>3</sup> month<sup>−1</sup> (n = 3). No evident fractures occurred in the Zn alloy scaffolds at 4 and 12 weeks after implantation. Hence, Zn alloy scaffolds are capable of maintaining mechanical integrity and preventing early mechanical failure during bone healing.

To further locate the site of new bone formation, calcein fluorochrome labeling was performed. Histological and fluorescence microscopy photographs showed that mineralization could be deposited and grew alongside the curved surface of implants continuously, and more well-structured new bone around the Zn–Mg–Cu scaffold could be observed after 12 weeks of implantation, in contrast to the diffuse mineralization and inflammatory tissue in the control group (Fig. 7C–D). Consistent with calcein staining results, collagen fibers dyed bright red were formed at the material-tissue interfaces and grew into the gradient pores of Zn–Mg–Cu at 4 weeks and 12 weeks as revealed by Van Gieson staining (Fig. 7E).

Additionally, Zn–Mg and Zn–Mg–Cu implants both demonstrated good biocompatibility with no signs of osteolysis, deformity or dislocation. Three-dimensional images revealed distinct new bone formation and direct contact between the new bone and implants in both the Zn–Mg and Zn–Mg–Cu groups at 12 weeks, which were further confirmed by representative cross-sections of the implants. Compared with Zn–Mg group, no significant inflammatory cell aggregation or tissue lesions was observed around the Zn–Mg–Cu scaffold. Moreover, the red-dyed collagen fibers in Zn–Mg–Cu group exhibited enhanced growth into the metal scaffold along the surface with TPMS structure compared to those in other groups, which indicated that Zn–Mg–Cu alloys exhibited a significantly higher new bone area compared to both Zn–Mg and the control group without implants (Fig. S11). These results demonstrated that the topological structure with gradient pores ensured the biocompatibility and osteoconductivity of the Zn–Mg–Cu scaffolds in treating diabetic maxillofacial bone defects. Meanwhile, the incorporation of copper ions into the Zn–Mg–Cu scaffold did not result in any potential toxicity to surrounding tissue, thereby mitigating concerns regarding tissue disease or necrosis. Overall, the Zn–Mg–Cu scaffold has the potential to provide a more active healing process and quicker bone regeneration under the hyperglycemic microenvironment through the incorporation of Mg and Cu elements and gradient structure construction.

### 3. Discussion

The skeleton, as an organ of the body, heavily depends on glucose metabolism, as the differentiation and function of osteoblasts require energy consumption during bone remodeling processes. Glucose is transported into osteoblasts via GLUT1, promoting osteoblast differentiation. This interplay between osteogenesis-related genes and glucose uptake acts as an amplification mechanism, ensuring well-coordinated, timely osteoblast differentiation and proper bone formation throughout life [51]. Osteokines, such as osteocalcin (OC) and bone morphogenetic protein (BMP), which are actively involved in glucose metabolism, have been shown to decrease in simulated hyperglycemic environments or diabetic conditions [52]. The sensitivity of bone tissue to blood glucose

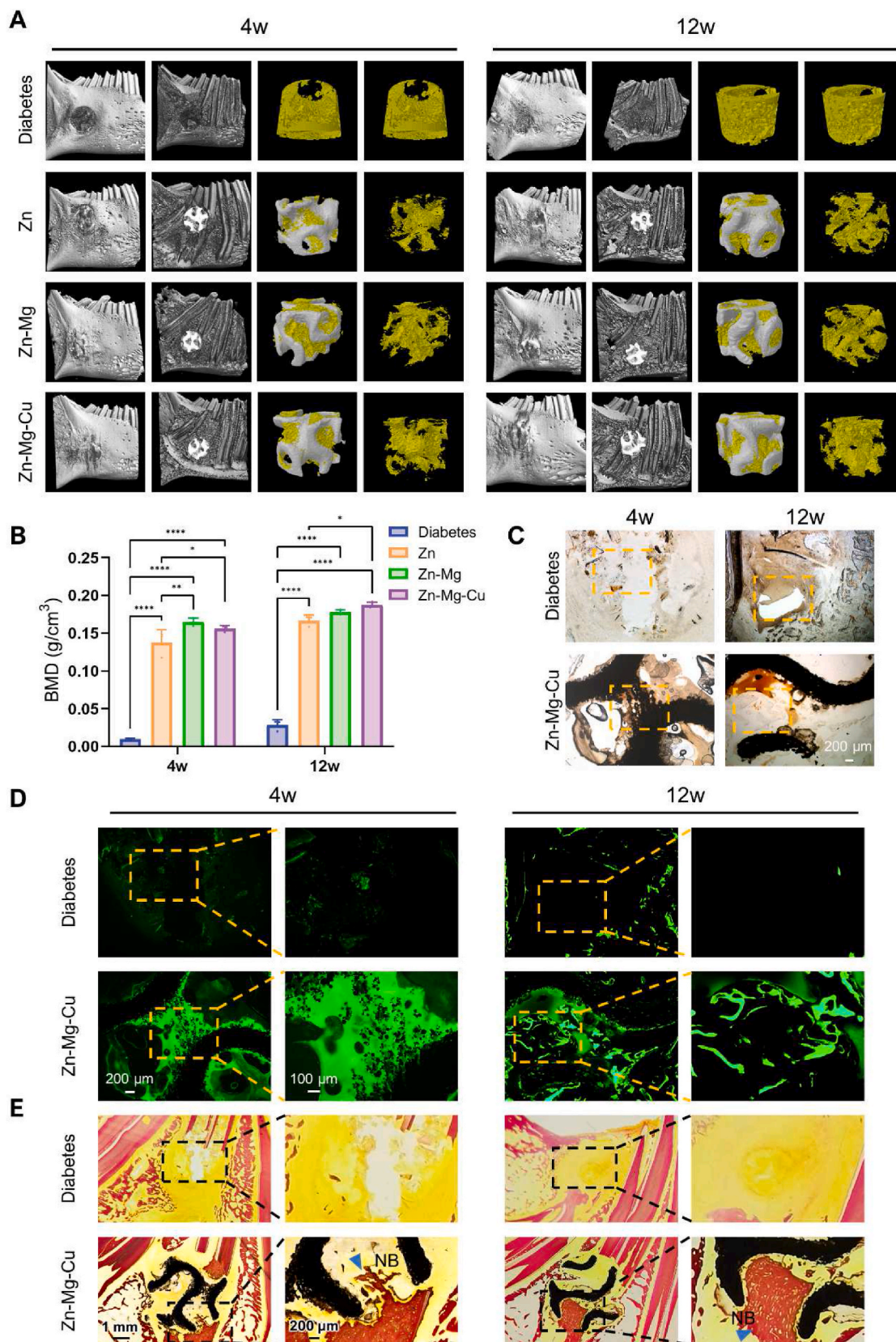


**Fig. 7.** *In vivo* evaluation of bone regeneration induced by Zn alloy scaffolds in diabetic rabbit mandibular defects. **A** Micro-CT 3D reconstruction image of the mandible and newly-formed bone with or without implants at week 4 and week 12. Implants are shown in white and new bone is shown in yellow. **B** Quantitative analysis of BMD analysis of the neo-bone within defects at 4 and 12 weeks after treatment, n = 3. The data are shown as the mean ± SD; \*P < 0.05, \*\*P < 0.01; \*\*\*P < 0.001 and \*\*\*\*P < 0.0001 indicate significant differences between the indicated columns. **C** Histological photographs (**C**) and representative images of calcein fluorochrome labeling (**D**) of bone tissue formed around and within Zn alloy implants at 4 weeks and 12 weeks. **E** Van Gieson staining at 4 weeks and 12 weeks (Blue triangles point to the newborn bone in direct contact with the implants).

was demonstrated in this study (Fig. 4C). Interestingly, the impaired osteoblast function caused by high glucose levels can be improved by Zn alloys, particularly Zn–Mg–Cu, as shown in this research. Furthermore, osteocalcin, the most abundant osteoblast-specific protein involved in glucose metabolism during bone formation, was increased in the presence of Zn–Mg–Cu. Consequently, this study suggests that the effect of Zn–Mg–Cu on osteogenesis may be associated with the glucose metabolism of osteoblasts [47].

Previous studies have reported associations between serum or bone concentrations of Zn, Mg, and Cu and metabolic disorders, especially those related to glucose metabolism. Supplementing with bioactive metal elements at suitable levels could help maintain metabolic homeostasis [20–22]. Moreover, lithium has been shown to have a therapeutic effect on glucose metabolic dysfunction by enhancing insulin-mediated glucose transport *in vitro* and restoring insulin sensitivity in animal models of insulin resistance [53]. Thus, it is reasonable to suggest that the slow release of metal ions from degradable metal scaffolds could enhance local osteoblast differentiation by promoting glucose uptake and subsequent cellular activities under high-glucose conditions.

RAC1 gene represents a novel genetic marker of type 2 diabetes and has been found to impact both glucose metabolism and disease pathogenesis. High glucose exposure led to the excessive activation of RAC1 and induced cell apoptosis [54]. Additionally, RAC1 has been reported to regulate osteoblast differentiation and bone formation by affecting the glucose uptake in osteoblasts [55]. In this study, we found that Zn–Mg–Cu could inhibit the expression of RAC1 induced by high glucose (Fig. 6E and Fig. S2A). Moreover, the glucose uptake ability of osteoblasts, the expression levels of glucose transporter Glut1, and vascular endothelial growth factor Vegfa were increased in the presence of Zn–Mg–Cu (Fig. 6F–G and Figs. S2D–E), which could partially explain the promoted osteoblast differentiation induced by Zn–Mg–Cu under high glucose environment. However, it is interesting to note that glucose uptake capacity and Glut1 expression of endothelial cells were also strengthened with the simulation of Zn–Mg–Cu (Figs. S2F–I), while qRT-PCR analysis revealed a reduction in RAC1 expression in HUVECs with Zn–Mg–Cu treatment (Fig. S2I). These findings suggest that Zn–Mg–Cu may operate through similar mechanisms to promote angiogenesis in endothelial cells.

The TPMS structure was used in the scaffold designation to mimic the unique hyperboloid topography of the trabecular bone, to induce a natural and tight integration with surrounding bone tissue. The hyperboloidal structure of TPMS structure was found to support the attachment and proliferation of human mesenchymal stem cells, and even guide the cell fate toward osteogenesis through cytoskeleton reorganization and nuclear deformation [23]. Zhang et al. also found that the scaffolds with graded porosity could facilitate the transport behavior of nutrients and metabolites, accompanying with a high-density distribution of cells and accelerated bone defect healing [56]. The gradient structure is more suitable for the mechanical environment of bone defects and provides a larger pore size range as compared to uniform structure, which benefits the material–bone interaction and the growth of new bone tissue. The drastic penetration and growth of new bone into the porous structure of Zn alloy implants shown in the present study (Fig. 7) also supported that the TPMS structure has the potential to augment bone formation. Moreover, compared with orthogonal lattice structure scaffolds, the highly relative surface areas and permeable cellular structures with sequential surfaces of TPMS facilitated the adequate contact between metal ions and cells [31,57], which further regulated cellular glucose metabolism in diabetic pathological environments. The material–structure–driven strategy of Zn–Mg–Cu gradient scaffolds achieved by additive manufacturing demonstrated favorable mechanical and biological performances, as evidenced by the enhanced bone regeneration in mandibular defects of diabetic rabbits. In summary, this study offers a potential approach for diabetic bone regeneration by mitigating cellular dysfunction caused by underlying metabolic

disorders, primarily using material–structure–driven bone scaffolds.

#### 4. Conclusions

In summary, we developed a material–structure–driven strategy for diabetic maxillofacial bone regeneration by additive manufacturing of degradable Zn–Mg–Cu gradient scaffolds. The scaffolds presented favorable mechanical strength and uniform degradation mode by *in situ* alloying of Mg and Cu with boundary engineering strategy. The simultaneous release of dual metal ions facilitated bacterial elimination and the proliferation of osteoblasts and endothelial cells in mimicked hyperglycemic microenvironment, thereby exhibiting favorable osteogenic and angiogenic abilities *in vitro*. Moreover, the biomimetic topography and suitable permeability of the gradient structure enhanced the osteoconductivity during the bone healing process, which improved new bone ingrowth and formation in the mandibular defect models of diabetic rabbits. Mechanism investigation suggests that RAC1-mediated glucose metabolism regulation may be the underlying molecular signal. Overall, our work directs the clinical use potential of the gradient Zn–Mg–Cu scaffolds for treating diabetic maxillofacial bone defects.

#### Ethics approval and consent to participate

All experimental procedures were approved by the Animal Research Committee of the Huazhong University of Science and Technology Tongji Medical College (Wuhan, China), according to the approved guideline (IACUC: 3336).

#### Declaration of competing interest

The authors declare that they have no known competing financial interests or personal relationships that could have appeared to influence the work reported in this paper.

#### CRediT authorship contribution statement

**Wencheng Song:** Writing – review & editing, Writing – original draft, Supervision, Methodology, Investigation, Formal analysis, Data curation. **Danlei Zhao:** Writing – review & editing, Writing – original draft, Supervision, Funding acquisition, Formal analysis, Data curation. **Fengyuan Guo:** Supervision, Methodology, Investigation. **Jiajia Wang:** Writing – original draft, Software, Methodology. **Yifan Wang:** Writing – review & editing, Methodology, Data curation. **Xinyuan Wang:** Software, Methodology, Formal analysis, Data curation. **Zhengshuo Han:** Software, Methodology, Data curation. **Wenjie Fan:** Methodology, Investigation, Data curation. **Yijun Liu:** Methodology, Data curation. **Zhi Xu:** Writing – review & editing, Supervision, Formal analysis. **Lili Chen:** Writing – review & editing, Supervision, Project administration, Funding acquisition.

#### Acknowledgements

The authors disclosed receipt of the following financial support for the research, authorship, and/or publication of this article: This research was supported by the National Natural Science Foundation of China for Key Program Projects (82030070, to L.C.) and the China Postdoctoral Science Foundation (2022TQ0110, 2023M731215 to D.Z.).

#### Appendix A. Supplementary data

Supplementary data to this article can be found online at <https://doi.org/10.1016/j.bioactmat.2024.06.028>.

## References

- [1] L.C. Hofbauer, B. Busse, R. Eastell, et al., Bone fragility in diabetes: novel concepts and clinical implications, *Lancet Diabetes Endocrinol.* 10 (3) (2022) 207–220.
- [2] P. Zhang, H. Zhang, J. Lin, et al., Insulin impedes osteogenesis of BMSCs by inhibiting autophagy and promoting premature senescence via the TGF- $\beta$ 1 pathway, *Aging (Albany NY)* 12 (3) (2020) 2084–2100.
- [3] B. Valdez-Salas, S. Castillo-Urbe, E. Beltran-Partida, et al., Recovering osteoblast functionality on TiO<sub>2</sub> nanotube surfaces under diabetic conditions, *Int. J. Nanomed.* 17 (2022) 5469–5488.
- [4] S.S. Hammer, C.P. Vieira, D. McFarland, et al., Fasting and fasting-mimicking treatment activate SIRT1/LXR $\alpha$  and alleviate diabetes-induced systemic and microvascular dysfunction, *Diabetologia* 64 (7) (2021) 1674–1689.
- [5] X.F. Hu, G. Xiang, T.J. Wang, et al., Impairment of type H vessels by NOX2-mediated endothelial oxidative stress: critical mechanisms and therapeutic targets for bone fragility in streptozotocin-induced type 1 diabetic mice, *Theranostics* 11 (8) (2021) 3796–3812.
- [6] R.A. Wimmer, A. Leopoldi, M. Aichinger, et al., Human blood vessel organoids as a model of diabetic vasculopathy, *Nature* 565 (7740) (2019) 505–510.
- [7] J. Guo, H. Yao, X. Li, et al., Advanced Hydrogel systems for mandibular reconstruction, *Bioact. Mater.* 21 (2023) 175–193.
- [8] M. He, H. Wang, Q. Han, et al., Glucose-primed PEEK orthopedic implants for antibacterial therapy and safeguarding diabetic osseointegration, *Biomaterials* 303 (2023) 122355.
- [9] S. Li, H. Yang, X. Qu, et al., Multiscale architecture design of 3D printed biodegradable Zn-based porous scaffolds for immunomodulatory osteogenesis, *Nat. Commun.* 15 (1) (2024) 3131.
- [10] Y. Lv, B. Wang, G. Liu, et al., Metal material, properties and design methods of porous biomedical scaffolds for additive manufacturing: a review, *Front. Bioeng. Biotechnol.* 9 (2021) 641130.
- [11] X. Wang, A. Liu, Z. Zhang, et al., Additively manufactured Zn-2Mg alloy porous scaffolds with customizable biodegradable performance and enhanced osteogenic ability, *Adv. Sci.* 11 (5) (2024) e2307329.
- [12] S. Lin, G. Yang, F. Jiang, et al., A magnesium-enriched 3D culture system that mimics the bone development microenvironment for vascularized bone regeneration, *Adv. Sci.* 6 (12) (2019) 1900209.
- [13] W. Qiao, K. Wong, J. Shen, et al., TRPM7 kinase-mediated immunomodulation in macrophage plays a central role in magnesium ion-induced bone regeneration, *Nat. Commun.* 12 (1) (2021) 2885.
- [14] E. Xiao, M. Mattos, G. Vieira, et al., Diabetes enhances IL-17 expression and alters the oral microbiome to increase its pathogenicity, *Cell Host Microbe* 22 (1) (2017) 120–128.
- [15] B. Li, R. Shu, W. Dai, et al., Bioheterojunction-engineered polyetheretherketone implants with diabetic infectious micromilieu twin-engine powered disinfection for boosted osteogenicity, *Small* 18 (45) (2022) e2203619.
- [16] B. Marelli, D. Le Nihouannen, S.A. Hacking, et al., Newly identified interfibrillar collagen crosslinking suppresses cell proliferation and remodelling, *Biomaterials* 54 (2015) 126–135.
- [17] C. Gerard, L.J. Bordeleau, J. Barralet, et al., The stimulation of angiogenesis and collagen deposition by copper, *Biomaterials* 31 (5) (2010) 824–831.
- [18] M. Liu, L. Huang, X. Xu, et al., Copper doped carbon dots for addressing bacterial biofilm formation, wound infection, and tooth staining, *ACS Nano* 16 (6) (2022) 9479–9497.
- [19] R. Liu, Y. Tang, L. Zeng, et al., In vitro and in vivo studies of anti-bacterial copper-bearing titanium alloy for dental application, *Dent. Mater.* 34 (8) (2018) 1112–1126.
- [20] C.W. Lu, Y.C. Lee, C.S. Kuo, et al., Association of serum levels of zinc, copper, and iron with risk of metabolic syndrome, *Nutrients* 13 (2) (2021).
- [21] J.C. Fernandez-Cao, M. Warthon-Medina, M.V. H, et al., Zinc intake and status and risk of type 2 diabetes mellitus: a systematic review and meta-analysis, *Nutrients* 11 (5) (2019).
- [22] A. Ryl, A. Szylińska, A. Bohatyrewicz, et al., Relationships between indicators of metabolic disorders and selected concentrations of bioelements and lead in serum and bone tissue in aging men, *Diabetes Metab Syndr Obes* 15 (2022) 3901–3911.
- [23] Y. Yang, T. Xu, H.P. Bei, et al., Gaussian curvature-driven direction of cell fate toward osteogenesis with triply periodic minimal surface scaffolds, *Proc. Natl. Acad. Sci. U. S. A.* 119 (41) (2022) e2088283177.
- [24] S.M. Ahmadi, R. Hedayati, Y. Li, et al., Fatigue performance of additively manufactured meta-biomaterials: the effects of topology and material type, *Acta Biomater.* 65 (2018) 292–304.
- [25] A.A. Zadpoor, Mechanical performance of additively manufactured meta-biomaterials, *Acta Biomater.* 85 (2019) 41–59.
- [26] L. Zhang, B. Wang, B. Song, et al., 3D printed biomimetic metamaterials with graded porosity and tapering topology for improved cell seeding and bone regeneration, *Bioact. Mater.* 25 (2023) 677–688.
- [27] S.L. Sing, J. An, W.Y. Yeong, et al., Laser and electron-beam powder-bed additive manufacturing of metallic implants: a review on processes, materials and designs, *J. Orthop. Res.* 34 (3) (2016) 369–385.
- [28] F. Bobbert, K. Lietaert, A.A. Eftekhari, et al., Additively manufactured metallic porous biomaterials based on minimal surfaces: a unique combination of topological, mechanical, and mass transport properties, *Acta Biomater.* 53 (2017) 572–584.
- [29] A. Pattnaik, A.S. Sanket, S. Pradhan, et al., Designing of gradient scaffolds and their applications in tissue regeneration, *Biomaterials* 296 (2023) 122078.
- [30] D. Zhao K.Y.T.S., Material structure function integrated additive manufacturing of degradable metallic, *Adv. Funct. Mater.* (2023).
- [31] L.M.X.J. Qiang Zhang, High-strength hydroxyapatite scaffolds with minimal surface macrostructures for load-bearing bone regeneration, *Adv. Funct. Mater.* 33 (2022) 2213128.
- [32] L.C. Gerhardt, K.L. Widdows, M.M. Erol, et al., The pro-angiogenic properties of multi-functional bioactive glass composite scaffolds, *Biomaterials* 32 (17) (2011) 4096–4108.
- [33] E. Alabort, D. Barba, R.C. Reed, Design of metallic bone by additive manufacturing, *Scripta Mater.* 164 (2019) 110–114.
- [34] J. Gao, Y. Su, Y.X. Qin, Calcium phosphate coatings enhance biocompatibility and degradation resistance of magnesium alloy: correlating in vitro and in vivo studies, *Bioact. Mater.* 6 (5) (2021) 1223–1229.
- [35] F. Bobbert, K. Lietaert, A.A. Eftekhari, et al., Additively manufactured metallic porous biomaterials based on minimal surfaces: a unique combination of topological, mechanical, and mass transport properties, *Acta Biomater.* 53 (2017) 572–584.
- [36] T. Albrektsson, B. Chrcanovic, P.O. Ostman, et al., Initial and long-term crestal bone responses to modern dental implants, *Periodontol* 73 (1) (2000, 2017) 41–50.
- [37] H. Chouirfa, H. Bouloussa, V. Migonney, et al., Review of titanium surface modification techniques and coatings for antibacterial applications, *Acta Biomater.* 83 (2019) 37–54.
- [38] H. Lu, Y. Liu, J. Guo, et al., Biomaterials with antibacterial and osteoinductive properties to repair infected bone defects, *Int. J. Mol. Sci.* 17 (3) (2016) 334.
- [39] J. Tuckermann, R.H. Adams, The endothelium-bone axis in development, homeostasis and bone and joint disease, *Nat. Rev. Rheumatol.* 17 (10) (2021) 608–620.
- [40] S.K. Ramasamy, A.P. Kusumbe, L. Wang, et al., Endothelial Notch activity promotes angiogenesis and osteogenesis in bone, *Nature* 507 (7492) (2014) 376–380.
- [41] J. Filipowska, K.A. Tomaszewski, L. Niedzwiedzki, et al., The role of vasculature in bone development, regeneration and proper systemic functioning, *Angiogenesis* 20 (3) (2017) 291–302.
- [42] L. Mao, L. Xia, J. Chang, et al., The synergistic effects of Sr and Si bioactive ions on osteogenesis, osteoclastogenesis and angiogenesis for osteoporotic bone regeneration, *Acta Biomater.* 61 (2017) 217–232.
- [43] A. Georgescu, Vascular dysfunction in diabetes: the endothelial progenitor cells as a new therapeutic strategy, *World J. Diabetes* 2 (6) (2011) 92–97.
- [44] U. Stucki, J. Schmid, C.F. Hammerle, et al., Temporal and local appearance of alkaline phosphatase activity in early stages of guided bone regeneration. A descriptive histochemical study in humans, *Clin. Oral Implants Res.* 12 (2) (2001) 121–127.
- [45] D.J. Rickard, M. Kassem, T.E. Hefferan, et al., Isolation and characterization of osteoblast precursor cells from human bone marrow, *J. Bone Miner. Res.* 11 (3) (1996) 312–324.
- [46] F.Y. Cao, J.X. Fan, Y. Long, et al., A smart fluorescence nanoprobe for the detection of cellular alkaline phosphatase activity and early osteogenic differentiation, *Nanomedicine* 12 (5) (2016) 1313–1322.
- [47] S.C. Moser, B. van der Eerden, Osteocalcin-A versatile bone-derived hormone, *Front. Endocrinol.* 9 (2018) 794.
- [48] T.G. Ebrahimian, C. Heymes, D. You, et al., NADPH oxidase-derived overproduction of reactive oxygen species impairs postischemic neovascularization in mice with type 1 diabetes, *Am. J. Pathol.* 169 (2) (2006) 719–728.
- [49] O.N. Bae, J.M. Wang, S.H. Baek, et al., Oxidative stress-mediated thrombospondin-2 upregulation impairs bone marrow-derived angiogenic cell function in diabetes mellitus, *Arterioscler. Thromb. Vasc. Biol.* 33 (8) (2013) 1920–1927.
- [50] H. Yang, B. Jia, Z. Zhang, et al., Alloying design of biodegradable zinc as promising bone implants for load-bearing applications, *Nat. Commun.* 11 (1) (2020) 401.
- [51] J. Wei, J. Shimazu, M.P. Makinistoglu, et al., Glucose uptake and Runx2 synergize to orchestrate osteoblast differentiation and bone formation, *Cell* 161 (7) (2015) 1576–1591.
- [52] B. Lecka-Czernik, Diabetes, bone and glucose-lowering agents: basic biology, *Diabetologia* 60 (7) (2017) 1163–1169.
- [53] I.H. Campbell, H. Campbell, D.J. Smith, Insulin signaling as a therapeutic mechanism of lithium in bipolar disorder, *Transl. Psychiatry* 12 (1) (2022) 350.
- [54] I. Azarova, E. Klyosova, A. Polonikov, Association between RAC1 gene variation, redox homeostasis and type 2 diabetes mellitus, *Eur. J. Clin. Invest.* 52 (8) (2022) e13792.
- [55] E. Esen, J. Chen, C.M. Karner, et al., WNT-LRP5 signaling induces Warburg effect through mTORC2 activation during osteoblast differentiation, *Cell Metabol.* 17 (5) (2013) 745–755.
- [56] L. Zhang, B. Wang, B. Song, et al., 3D printed biomimetic metamaterials with graded porosity and tapering topology for improved cell seeding and bone regeneration, *Bioact. Mater.* 25 (2023) 677–688.
- [57] B.L.S.A. Dorien Van Hede, 3D-Printed synthetic hydroxyapatite scaffold with in silico optimized macrostructure enhances bone formation in vivo, *Adv. Funct. Mater.* (2021).